One-Pot Aqueous Synthesis of Hierarchical $Na_3V_2(PO_4)_3$ (NVP) Particles for High-Performance Sodium Batteries

Ethan Boutelle[‡], Arden Chen[‡], Rajeev Gopal, and Peng Bai.*

[‡]These authors contributed equally

Corresponding Author

Peng Bai *– Department of Energy, Environmental and Chemical Engineering, Washington University in St. Louis, St. Louis, Missouri 63130, United States; Institute of Materials Science and Engineering, Washington University in St. Louis, St. Louis, Missouri 63130, United States; orcid.org/0000-0002-2419-3498; Email: pbai@wustl.edu*

Authors

Ethan Boutelle *– Department of Energy, Environmental and Chemical Engineering, Washington University in St. Louis, St. Louis, Missouri 63130, United States*

Arden Chen *– Department of Energy, Environmental and Chemical Engineering, Washington University in St. Louis, St. Louis, Missouri 63130, United States*

Rajeev Gopal *– Department of Energy, Environmental and Chemical Engineering, Washington University in St. Louis, St. Louis, Missouri 63130, United States*

Department of Energy, Environmental & Chemical Engineering, Washington University in Saint Louis

1 Brookings Dr., St. Louis, MO 63130, USA

Abstract

Intermittent renewable energy sources can mitigate climate change, but they require high-performance, reliable batteries. The widely used lithium-ion batteries contain Li, Co, and Ni, and the growing demand for these elements, together with their relatively few sources, has raised concerns about their supply chain stability. Sodium-ion batteries have become an economical alternative. Sodium vanadium phosphate, $Na_3V_2(PO_4)_3$ (NVP), is a compelling candidate with high stability and ionic conductivity due to its polyanionic sodium superionic conductor (NASICON) structure. However, NVP suffers from poor electronic conductivity and requires hierarchical morphology to allow facile ion and electron transfer. Spray-drying has been used to achieve hierarchical secondary particle structures, but the foremost reported NVP syntheses rely on either flammable/toxic organic solvents or expensive nanocarbon additives. In this study, we spray-dry an aqueous suspension without using expensive carbon additives. The obtained NVP sodium-ion half cells showed very high reversible capacity (114.7 mAh g^{-1} at 0.2C), high rate capability (80.8% capacity retention at 30C), and stable cycling performance (96.7% capacity retention after 1,500 cycles at 10C). This superior performance demonstrates the great promise for NVP batteries as an alternative energy storage option to traditional lithium-ion batteries.

Introduction

Worldwide electricity demand, mostly satisfied through coal and natural gas combustion, is expected to double by the middle of the century.[1] Renewable energy sources are becoming increasingly crucial as climate change presents more urgent challenges. However, their inherent variability necessitates reliable, long-lasting energy storage. Due to their energy density and longevity, lithium-ion batteries (LIBs) have become the industry standard, but the depletion of sources of lithium and associated cathode materials, such as cobalt and nickel, has led to higher costs and greater environmental production concerns.[2–4] Sodium-ion batteries (NIBs) are a promising alternative because the abundance of sodium and associated cathode materials results in lower cost and less environmental impact.[5–8] NIBs particularly excel in grid-

scale energy storage, because stationary storage prioritizes cheap and long-lasting batteries over the high energy density provided by lithium-ion batteries. However, improvements are still needed before NIBs can be widely adopted or considered a competitive alternative to LIBs, and cathode active materials particularly limit performance.[9] Among the three major choices, layered metal oxides (LMOs), despite the high specific capacity,[10,11] still need to prove their electrochemical longevity and air stability in a cost-effective manner.[12] Prussian Blue Analogues (PBAs), while enjoying the cost advantage,[13] need to demonstrate precision control of vacancies and interstitial water that undermine cycle life significantly.[14–18] Polyanion cathode materials have demonstrated excellent cycle life owing to their intrinsically stable crystal structures, which potentially lowers the service-life cost to a more competitive level than other choices.[19,20]

Sodium vanadium phosphate (NVP, $Na_3V_2(PO_4)_3$) is one of the most promising polyanionic NIB cathode materials with a rhombohedral sodium superionic conductor (NASICON) structure that provides rapid Na^+ ion conductivity while maintaining a stable intercalation framework. It offers a theoretical capacity of 118 mAh g^{-1} and high thermal stability.[21] However, NVP has a low electronic conductivity (1.63×10^{-6} S cm^{-1}) which can limit electrochemical performance.[22,23] This limitation can be alleviated by carbon coating, through in-situ or post-synthesis techniques, while maintaining a porous and stable material.[24] Unfortunately, common synthesis routes that produce high-performance powders face challenges.[25] For example, when the sol-gel and hydrothermal methods are combined, a slurry or gel of precursor salts is prepared under hydrothermal conditions, dried to obtain the precursor powder, and finally calcinated.[26–29] These methods have precise control of reaction conditions and yield inherently small primary particles, allowing for precise control over particle morphology. However, the sol-gel method is complex and costly while the hydrothermal step has a low yield, making them difficult to scale-up.[30,31] Similarly, electrospinning a viscous slurry of NVP precursors allows for precise morphology control but is difficult to scale due to a low flow rate through a fine needle.[32–34] Solid-state synthesis methods have been demonstrated, in which precursor salts are directly combined and milled, then

calcinated.[35,36] This method is easily scalable and similar techniques have been used in industrial settings, but undesirable morphology and the presence of impurity phases make it unattractive.[31]

Alternatively, the spray-drying method is widely used in the battery materials production industry. For NVP synthesis, a precursor suspension is spray-dried to obtain spherical secondary particles, followed by calcination to obtain the final NVP product.[37] The particle sizes, thickness of the carbon coating, and overall morphology are easily tuned through manipulation of concentration, temperature, and carbon additives. It is also a quick process performed at moderate temperatures that yields uniform precursor powders, thus is easily scalable.[31] However, the most successful NVP spray-drying results have either required flammable organic solvents such as methanol[38] which then require a sophisticated inert-gas spray dryer, or used expensive nanocarbon additives such as graphene or carbon nanotubes,[39,40] both of which significantly increase production costs. For scaled-up synthesis, it is highly preferable to avoid expensive additives and hazardous solvents that impose high safety risks or high processing costs.[41]

Herein, we have developed a one-pot *aqueous* spray-drying process to replace traditional methods of synthesizing carbon-coated NVP (NVP-C). The process is easily scaled for industrial applications, and the synthesized samples demonstrate high-rate performance, near-theoretical capacity, and a long working lifespan. This study highlights the very high potential for NVP-C as a cathode material for sustainable, reliable, and cost-efficient batteries.

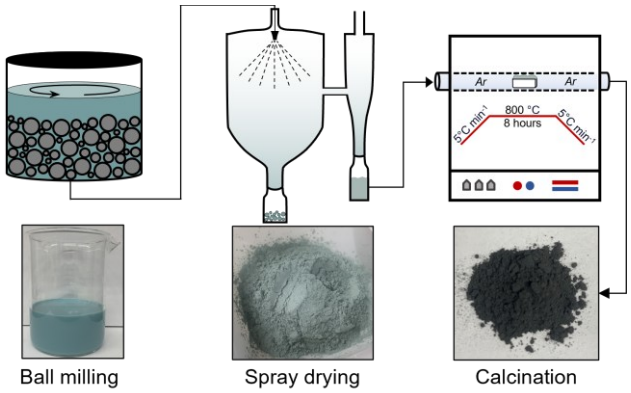

Figure 1. Schematic of the one-pot NVP-C synthesis, consisting of ball milling, spray-drying, and calcination.

Experimental Materials and Methods

Synthesis

NVP-C microspheres were synthesized through ball milling, spray-drying, and subsequent calcination. As shown in Figure 1, 22.46g of NaH_2PO_4, 8.72g of V_2O_5, and 4.67g of $C_6H_8O_6$ were added to 200 mL of de-ionized water, and then ball milled with zirconium balls for 4 hours, alternating 5 minutes of milling with 5 minutes of rest. The resulting opaque turquoise suspension was rested overnight, then diluted with 100 mL of water to reduce clogging during spraying. The constantly mixed suspension was spray-dried at either 150°C (NVP-150R) to reduce the energy consumption of the process, or 210°C (NVP-210R) for comparison with previous reports.[38,39] Another sample was diluted and sprayed at 150°C immediately after ball milling without resting overnight (NVP-150). The collected powder was calcinated at 800°C in an argon atmosphere at a heating rate of 5°C min^{-1} and a soaking time of 8 hours, before the final NVP-C product was obtained. Based on the initial precursor mass, the final product yields were between 75% and 80% due to particles bonding to the wall of the main spray-dryer chamber.

Material Characterization

X-ray diffraction (XRD) was performed with a Bruker D8 Advance powder diffraction system. A Thermofisher Quattro S ESEM microscope was used for scanning electron microscopy. Thermogravimetric analysis (TGA) was performed on a TA Instruments Q5000 Automatic Sample Processor under an air atmosphere to determine the final carbon content of the powder. Raman spectroscopy was performed using a Renishaw inVia Raman microscope with an excitation wavelength of 532nm. Brunauer-Emmett-Teller (BET) surface area analysis was completed on a Quantachrome Nova 2000e after degassing the sample overnight at 300°C.

Electrochemical Performance

The electrochemical performance of the obtained NVP-C microspheres was determined with Na-ion half-cells using CR2025 coin cell cases. Low-loading NVP-C cathodes were made using a traditional slurry composed of 80 wt.% NVP powder, 10 wt.% HSV900 PVDF binder (MTI), and 10 wt.%

Ketjenblack EC-300J (Fuelcell Store) or EC-600JD (MSE supplies) in sufficient N-methyl-2-pyrrolidone (NMP) solvent. The slurry was mixed in a vortex mixer and coated onto aluminum foil before being dried in a convection oven at 80°C. Electrodes were cut into 8mm diameter circles and vacuum dried at 120°C overnight. Active material loading was maintained between 0.5 - 1 mg cm^{-2}. High-loading NVP-C cathodes (active material loading 13.50 mg cm^{-2}) were made with 80 wt.% NVP powder, 15 wt.% HSV900 PVDF binder (MTI), and 5 wt.% Ketjenblack EC-600JD (MSE supplies). Na-ion half-cells were constructed with NVP-C as the cathode, a PP-PE-PP trilayer separator (Celgard), and a sodium metal counter electrode. The electrolyte was 1M $NaPF_6$ in diglyme. A LAND CT2001A battery testing system was used to evaluate the constant-current electrochemical cycling performance of the cells. Cyclic voltammetry was performed using a Gamry 600+ potentiostat.

Results and Discussion

This procedure demonstrates a quick, sustainable one-pot method for synthesizing NVP-C using water as a solvent. In this method, L-ascorbic acid chemically reduces the vanadium pentoxide in the precursor slurry, increasing its solubility and milling efficiency, resulting in a turquoise spray-dried product (Fig. 1). Thus, L-ascorbic acid simultaneously ensures the formation of a homogeneous precursor powder from an aqueous slurry while providing a simple inexpensive carbon source for the final calcinated product.

Three NVP-C products were synthesized. For two syntheses, the ball-milled slurry was allowed to rest overnight before dilution and spray-drying. The first product was spray-dried at 210°C (NVP-210R), while another was spray-dried at 150°C to reduce energy consumption (NVP-150R). The final material was diluted immediately after ball milling to determine the effect of resting the slurry before dilution (NVP-150). The spray-drying synthesis created small droplets of colloidal suspension that dried quickly, yielding spherical particles between 3 and 30 μm in diameter as shown in Figure 2(a-f). The addition of

L-ascorbic acid did not impede the formation of highly porous hierarchical particles and gave high yields from an aqueous slurry.

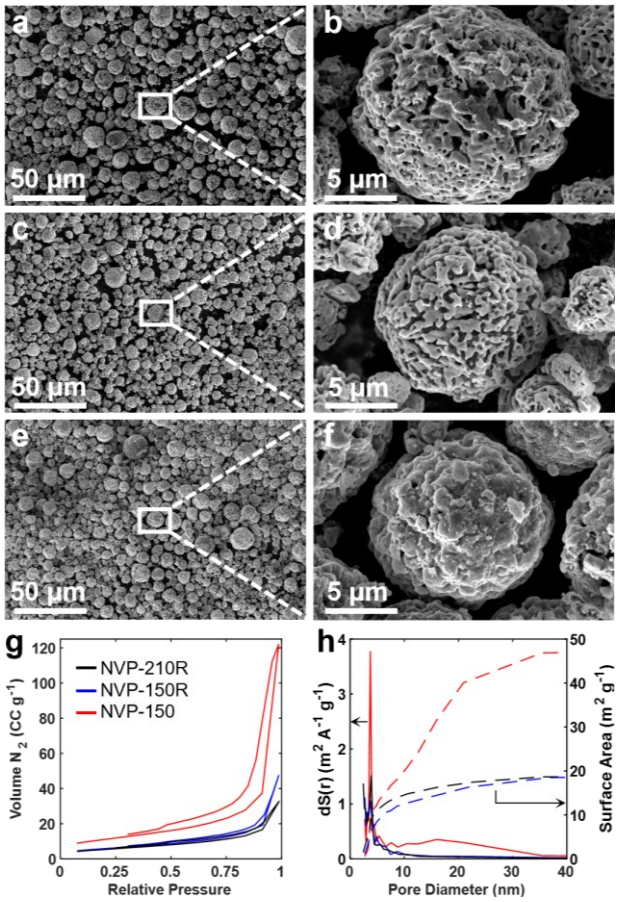

Figure 2. SEM images of the final NVP-C calcinated product (**a**,**b**) NVP-210R; (**c**,**d**) NVP- 150R; (**e**,**f**) NVP-150. (**g**) Nitrogen adsorption-desorption isotherms and (**h**) corresponding surface area pore size distributions of the three NVP-C materials.

Figure 2(g) shows isotherms of the three NVP-C materials. BET analysis indicates specific surface areas of 19.45 m^2g^{-1}, 21.09 m^2g^{-1}, and 39.55 m^2g^{-1} for NVP-210R, NVP-150R, and NVP-150, respectively. Although SEM images of NVP-150 appear less porous than the other materials, it is important to note the difference in scale between the micron-sized pores visible in SEM and the mesopores analyzed by BET which are under 50 nm. Repeatable BET tests indicate that NVP-150 has roughly double the specific surface area of the other materials, much of which is attributed to larger pores between 10-30 nm in diameter (Fig. 2(h)). Contrarily, most of the surface area of NVP-210R and NVP-150R is localized

to pores ~3.7 nm in diameter. We hypothesize that resting the slurry overnight allows for the formation of discrete vanadium-rich phases, resulting in larger primary particles and an overall lower porosity. Thus, diluting the slurry immediately maintains a homogeneous precursor, resulting in small primary particles with a wider pore size distribution and higher specific surface area. The tap densities of NVP-210R, NVP-150R, and NVP-150 and were estimated as 0.71 g/cm^3, 0.64 g/cm^3, and 0.67 g/cm^3, respectively.

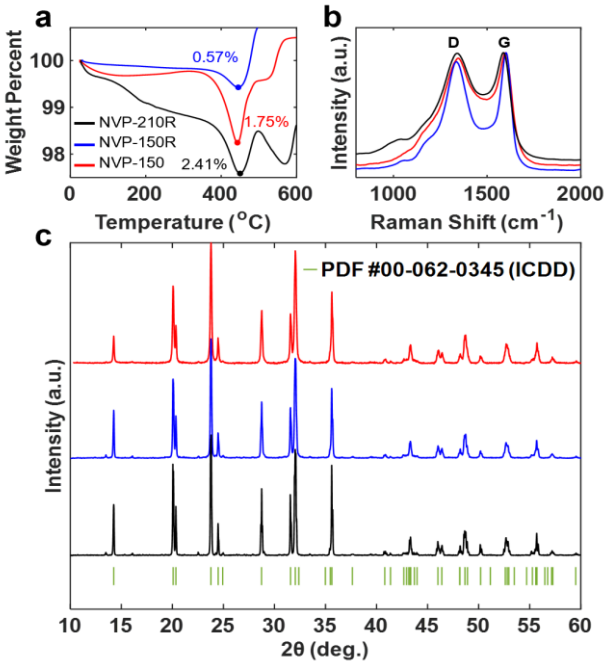

Figure 3. Physical characterization of the NVP-C samples. (**a**) TGA curves under an air atmosphere, providing approximate carbon contents. (**b**) Raman spectroscopy, with D and G bands labeled. (**c**) XRD patterns and Bragg positions from PDF card #00-062-0345 (ICDD).

As shown in Figure 3(c), XRD patterns for all samples demonstrate sharp peaks that are well-indexed to the rhombohedral PDF card #00-062-0345 (ICDD), indicating a highly crystalline lattice. As shown in Figure 3(b), the Raman spectra of all samples exhibit two characteristic bands centered at ~1345 cm^{-1} and ~1595 cm^{-1}, ascribed to the D-band (disordered) and G-band (graphitized) carbon. The intensity ratios of the peaks (I_D/I_G) are 0.93, 0.96, and 0.99 for NVP-150, NVP-150R, and NVP-210R, respectively, indicating that approximately half of the residual carbon was graphitized.

Figure 3(a) shows weight loss curves for TGA performed in a dry air atmosphere. The maximum weight losses, taken as the approximate carbon weight percentage, were 2.41 wt.% for NVP-210R, 0.57 wt.% for NVP-150R, and 1.75 wt.% for NVP-150. It should be noted that NVP has been demonstrated to oxidize under an air atmosphere above 500°C.[42] Thus, we attribute the fluctuations in the weight loss curves to the simultaneous combustion of the carbon coating and oxidation of the NVP lattice, which occur at different stages depending on the morphology of the sample. Combustion of the carbon coating dominates up to 450°C resulting in weight loss, followed by simultaneous oxidation of the NVP lattice causing the sample weight to increase. Admittedly, the obtained carbon percentages are approximate, but NVP-210R shows the highest carbon content, NVP-150 shows an intermediate carbon content, and NVP-150R shows the lowest carbon content.

To investigate the effect of the NVP-C carbon content on electrochemical kinetics, cathodes were cast with 10 wt.% of either Ketjenblack EC-300J or the more conductive EC-600JD and tested in half-cells.[43] The CV curves in Figure 4(a,d) were used to perform Randles-Sevcik analysis and extract apparent diffusion coefficients, D_{app}, using the following equation[44]:

$$i_p = 2.69 \times 10^5 n^{3/2} A C_{Na^+} \, {D_{app}}^{1/2} \nu^{1/2}. \qquad \text{Eq. (1)}$$

Here, i_p is the observed current response, n is the number of electrons transferred (two in this case), A is the electrode area, C_{Na^+} is the concentration of Na^+ ions in the NVP-C material (6.92×10^{-3} mol cm^{-3}, based on two mobile Na^+ ions), D_{app} is the apparent diffusion coefficient of Na^+ in NVP-C, and ν is the scan rate. For this study, D_{app} values (Table 1) were calculated using both the geometric area of the

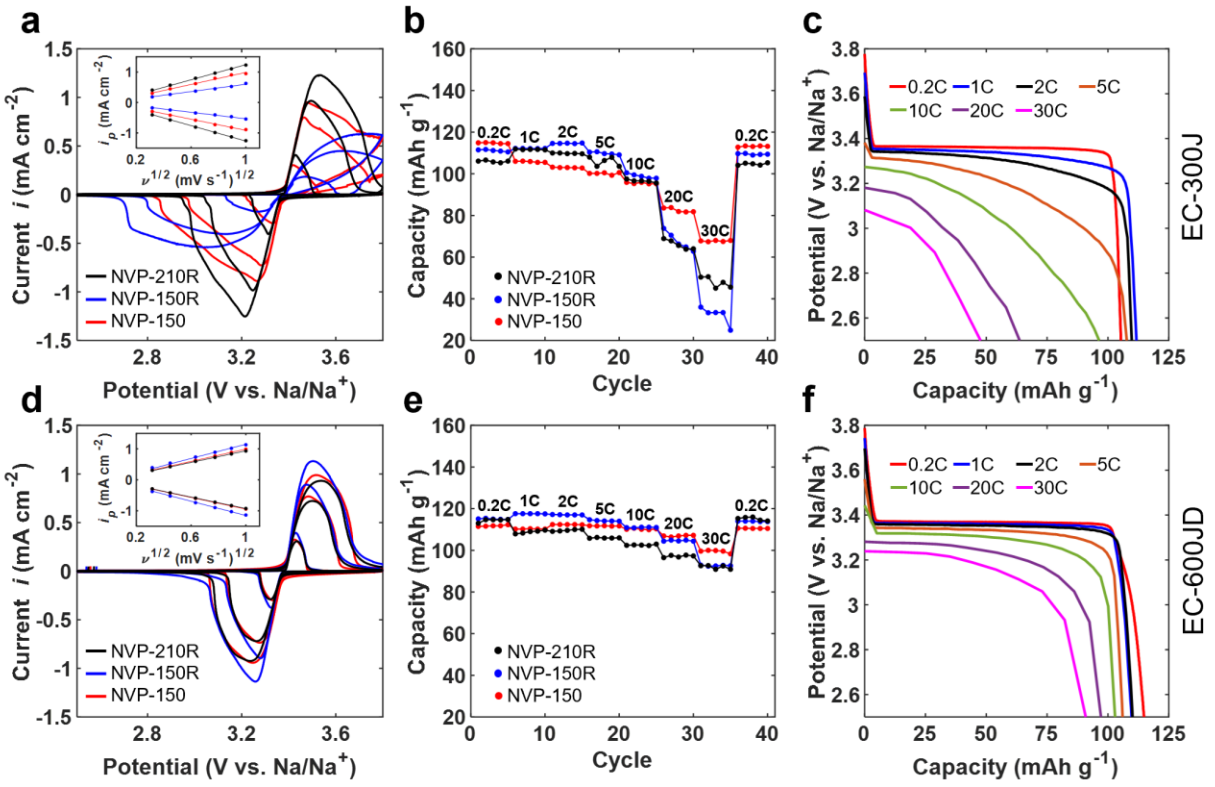

Figure 4. Electrochemical characterization of the prepared NVP-C materials in Na-ion half-cells. Cathodes were mixed with 10 wt.% Ketjenblack EC-300J (top) or EC-600JD (bottom). (**a**,**d**) Cyclic voltammetry curves at 0.1 mv s^{-1}, 0.6 mv s^{-1}, and 1 mv s^{-1}. Insets show the relationship of i_p and $\nu^{1/2}$. (**b**,**e**) Discharge specific capacity of all materials and (**c**,**f**) galvanostatic discharge profiles of NVP-210R during ramp tests at C rates of 0.2C, 1C, 2C, 5C, 10C, 20C, and 30C.

electrode (A_{geo}) as well as the surface area determined from BET testing (A_{BET}). Intuitively, A_{BET} should be used in Eq. (1), as it more accurately represents the interfacial area between the active material and the electrolyte. However, studies on intercalation porous electrodes have demonstrated that not all particles or interfacial areas react concurrently. Instead, an in-plane particle-by-particle process[45–49] and cross-plane layer-by-layer process [50–54] are observed, making A_{geo} a more reasonable choice to yield diffusion coefficients closer to density functional theory (DFT)[45]. Therefore, diffusion coefficients based on A_{BET} inevitably underestimate the true kinetics and must be used with caution as the lower limit. Likewise, those based on A_{geo} should be taken as upper limits. More accurate diffusion coefficients should be determined using an experimental setup where the actual active interfacial area can be determined.

Table 1. Apparent diffusion coefficients D_{app} in $cm^2\ s^{-1}$ for the three NVP-C materials mixed with Ketjenblack EC-300J or EC-600JD. Values were calculated using both the geometric area, $A_{geo,}$ and the BET determined surface area, $A_{BET.}$

Ketjenblack	Area	NVP-150R		NVP-150		NVP-210R	
		Charge	Discharge	Charge	Discharge	Charge	Discharge
EC-300J	A_{geo}	1.30×10^{-11}	1.03×10^{-11}	3.52×10^{-11}	3.01×10^{-11}	5.58×10^{-11}	5.78×10^{-11}
	A_{BET}	4.92×10^{-16}	3.91×10^{-16}	3.85×10^{-16}	3.29×10^{-16}	3.00×10^{-15}	3.11×10^{-15}
EC-600JD	A_{geo}	4.76×10^{-11}	4.78×10^{-11}	3.55×10^{-11}	3.23×10^{-11}	3.16×10^{-11}	3.10×10^{-11}
	A_{BET}	2.71×10^{-15}	2.72×10^{-15}	6.74×10^{-16}	6.13×10^{-16}	3.11×10^{-15}	3.06×10^{-15}

When mixed with Ketjenblack EC-300J, D_{app} values (calculated using A_{geo}) increase with carbon content, as $D_{app}{}^{\mathrm{NVP-150R}} < D_{app}{}^{\mathrm{NVP-150}} < D_{app}{}^{\mathrm{NVP-210R}}$. The shape of the CV curves also improves with increasing carbon content, demonstrating narrower and more symmetric peaks. Conversely, cathodes mixed with the more conductive Ketjenblack EC-600JD show the reverse trend, with D_{app} values decreasing with increasing carbon content. The corresponding CV curves all demonstrate narrow peaks and high symmetry. These results suggest that the high porosity of the samples allows for intimate contact with the electrolyte and enables facile ionic transport, while the low carbon content of the NVP-C materials creates an electronic limitation. When mixed with the less conductive Ketjenblack EC-300J, this electronic limitation is exacerbated; thus, increasing the carbon content of the NVP-C secondary particles alleviates this limitation and results in higher D_{app} values. When mixed with the more conductive Ketjenblack EC-600JD, this electronic limitation is removed and ionic transport through the carbon coating becomes the limiting kinetic factor, and samples with higher carbon contents demonstrate lower D_{app} values.

Discharge capacities during constant current ramp tests shown in Figure 4(b,e) corroborate this claim. All cells initially demonstrate a specific capacity close to the theoretical value of 118 mAh g^{-1} at 0.2C and

retain their capacity after cycling at high C-rates, indicating a robust material. A small but notable increase in specific capacity was observed across many cells during early cycling, which is attributed to the improved wetting of the porous cathode structure to achieve complete electrochemical activation in the first few cycles. This phenomenon was more pronounced for the samples with smaller pores (i.e. NVP-210R and NVP-150R) than for NVP-150 which has a wider pore-size distribution (Fig. 2h) that allows facile wetting of the cathode. When mixed with Ketjenblack EC-300J, NVP-150R demonstrates a lower specific capacity at high C-rates than NVP-210R. However, when mixed with Ketjenblack EC-600JD, the materials perform similarly, with NVP-150R showing a slightly better rate performance up to 20C. As a result of its broad pore size distribution and high surface area, NVP-150 shows the highest capacity at rates greater than 10C regardless of the conductive additive. There is clearly a tradeoff between ionic and electronic transport limitations in the NVP-C material, demonstrated by the discharge profiles of NVP-210R in Figure 4(c,f). When mixed with Ketjenblack EC-300J, discharge plateaus (vs. Na/Na^+) decrease from 3.35 V at 1C to 3.00 V at 30C. When mixed with Ketjenblack EC-600JD, the higher electronic conductivity reduces the overpotential and yields a discharge plateau at 3.23 V vs. Na/Na^+ at 30C. We can thus infer that although this material has the highest carbon content, electronic conductivity is still a limiting factor at high C-rates.

Figure 5 demonstrates the longevity of the NVP-C materials cycled at 10C between 2.5 V and 3.8 V vs. Na/Na^+. When cathodes are mixed with Ketjenblack EC-300J (Fig. 5(a,b)), NVP-210R clearly outperforms the other two samples because of its high carbon content, retaining 96.7% of its initial capacity after 1500 cycles while maintaining a coulombic efficiency near 100%. NVP-150 retains 88.7% of its initial capacity, while NVP-150R degrades quickly, with a final retention of 34.8%. Galvanostatic potential profiles during cycles 1, 1000, and 1500 also reflect this performance trend. During cycling, the overpotential for NVP-210R increases from 30 to 84 mV. On the other hand, the overpotential for NVP-150 increases from 95 to 189 mV, while NVP-150R shows the most dramatic increase, from 115 to 229 mV.

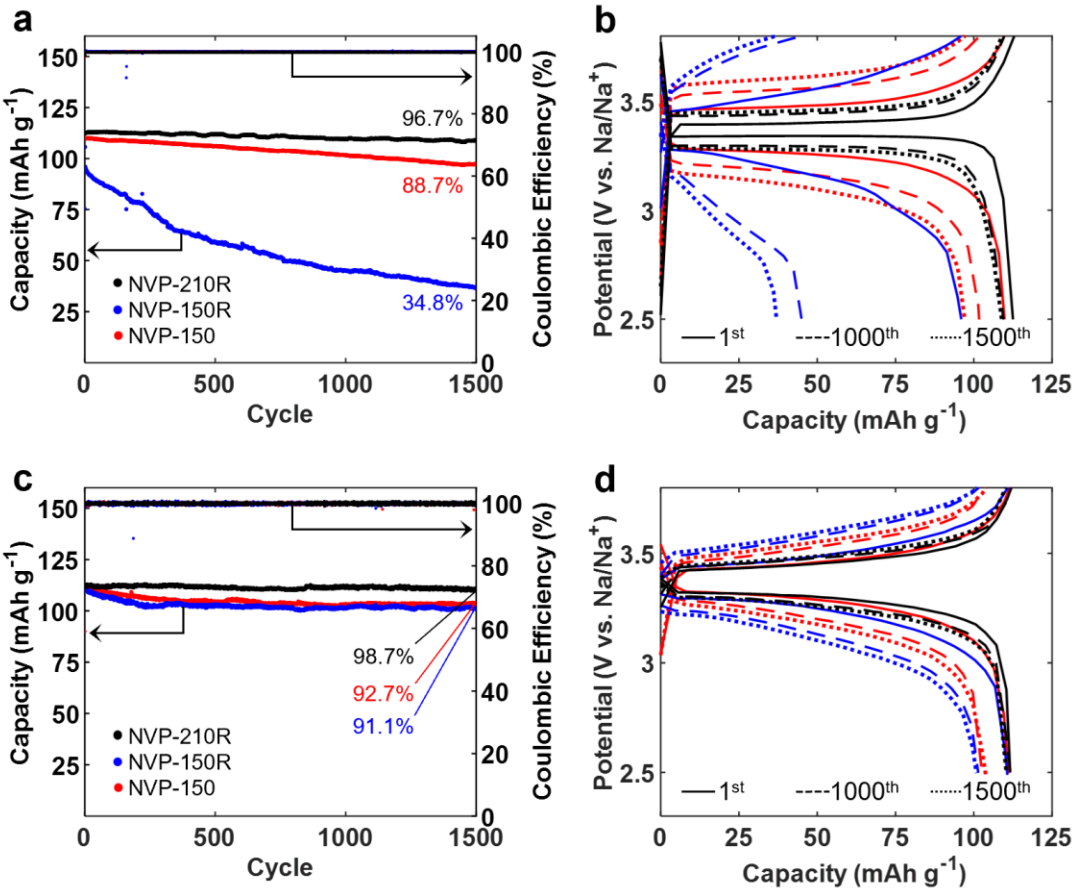

Figure 5. Long-term cycling of the three NVP-C materials at 10C mixed with Ketjenblack EC-300J (**a**,**b**) and Ketjenblack EC-600JD (**c**,**d**). (**a**,**c**) Discharge capacities and coulombic efficiencies and (**b**,**d**) galvanostatic potential profiles of the 1st, 1000th, and 1500th cycles.

Changing the electronic conductivity additive to Ketjenblack EC-600JD improves the performance of all three samples (Fig. 5(c,d)). NVP-150R demonstrates the most dramatic improvement, retaining 91.1% of its initial capacity, while overpotential increases from 75 to 155 mV. NVP-150 also shows significant improvement, with a final retention of 92.7% and an overpotential increase from 55 to 113 mV. Finally, NVP-210R demonstrates the highest retention of 98.7%, with a minimal overpotential increase from 55 mV to 73 mV. These low-loading cells can continue cycling at a similar degradation rate and easily complete thousands of cycles, demonstrating the ultimate electrochemical stability of the cathode material.

To demonstrate the efficacy of the NVP-C material in a more realistic setting, high-loading half-cells were constructed using NVP-210R. Figure 6(c,d) shows cycling data from a cell with an areal capacity of

1.33 mAh cm^{-2} (active material loading of 13.50 mg cm^{-2}) cycled at 0.5C. The cell had an initial discharge capacity of 91.5 mAh g^{-1}, which showed no degradation and increased to 98.8 mAh g^{-1} after 400 cycles while maintaining high coulombic efficiency. The low initial value and increase in specific capacity are attributed to the wetting of the cathode as cycling progresses, a phenomenon that is exacerbated in the high-loading cathodes. To further implement this material, high-loading slurry casting must be optimized to allow for full use of the active material. However, the voltage profiles of the high-capacity half-cell demonstrate an initial overpotential of 27.1 mV that barely increases to 31.6 mV. Such a small overpotential and stable cycling curves suggest that the NVP-210R material is not only suitable for small scale testing in coin cells but can also be used in realistic battery storage applications.

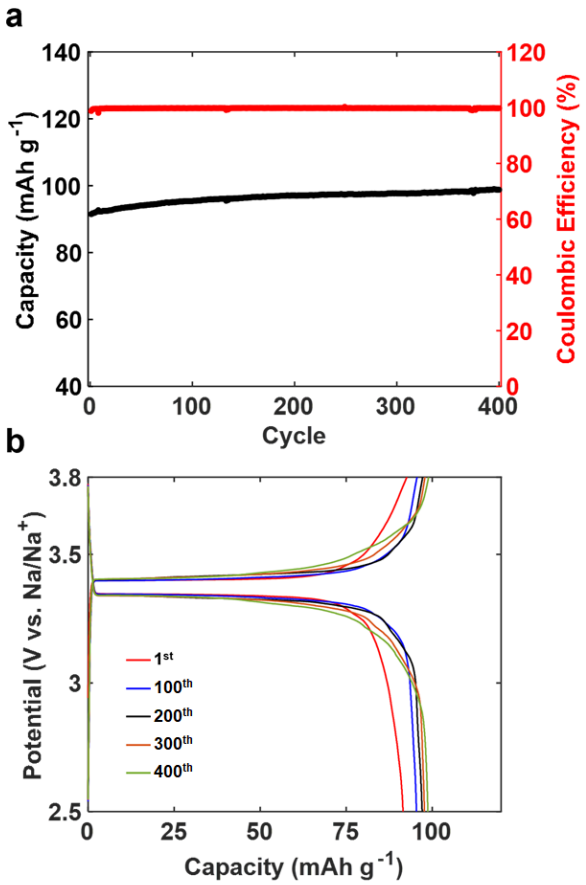

Figure 6. Cycling stability of high-loading NVP cathode (**a**) Discharge capacity and coulombic efficiency, and (**b**) voltage profiles of NVP-210R high-loading cathodes at 0.5C. Active material loading was 13.50 mg cm^{-2}.

Conclusions

An efficient and sustainable method for synthesizing porous NVP-C hierarchical particles with tunable carbon contents, without the use of organic solvents or expensive nanocarbon additives, was developed. The addition of L-ascorbic acid to an aqueous precursor slurry allowed for impressive yields, even at low spray-drying temperatures, of a high-performance material that exhibits near-theoretical capacity, high rate capability, and longevity. Low carbon content samples were shown to be limited by electronic conductivity, which may be alleviated by the addition of better conductive additives. In the future, the synthesis may be improved to further reduce its energy consumption and yield a more precise carbon content. This study has highlighted NVP-C as a viable inexpensive alternative to lithium-based batteries, particularly for large-scale stationary energy storage systems.

Acknowledgements: This work is partially supported by National Science Foundation grants (Award No. 2044932 and No. 2431923), a McKelvey Collaboration Initiation Grant (CIG) from Washington University, and a Research Gift from TSVC. The material characterization experiments were partially supported by IMSE (Institute of Materials Science and Engineering) at Washington University in Saint Louis.

References

(1) Yang, Z.; Zhang, J.; Kintner-Meyer, M. C. W.; Lu, X.; Choi, D.; Lemmon, J. P.; Liu, J. Electrochemical Energy Storage for Green Grid. *Chemical Reviews*. May 11, 2011, pp 3577–3613. https://doi.org/10.1021/cr100290v.

(2) Harper, G.; Sommerville, R.; Kendrick, E.; Driscoll, L.; Slater, P.; Stolkin, R.; Walton, A.; Christensen, P.; Heidrich, O.; Lambert, S.; Abbott, A.; Ryder, K.; Gaines, L.; Anderson, P. Recycling Lithium-Ion Batteries from Electric Vehicles. *Nature*. Nature Publishing Group November 7, 2019, pp 75–86. https://doi.org/10.1038/s41586-019-1682-5.

(3) Peters, J. F.; Weil, M. A Critical Assessment of the Resource Depletion Potential of Current and Future Lithium-Ion Batteries. *Resources* **2016**, *5* (4). https://doi.org/10.3390/resources5040046.

(4) *The Demand for Lithium-Ion*. www.nature.com/natrevmats.

(5) Liu, J. Addressing the Grand Challenges in Energy Storage. *Advanced Functional Materials*. February 25, 2013, pp 924–928. https://doi.org/10.1002/adfm.201203058.

(6) Yao, A.; Benson, S. M.; Chueh, W. C. *How Quickly Can Sodium-Ion Learn? Assessing Scenarios for Techno-Economic Competitiveness against Lithium-Ion Batteries*.

(7) Hirsh, H. S.; Li, Y.; Tan, D. H. S.; Zhang, M.; Zhao, E.; Meng, Y. S. Sodium-Ion Batteries Paving the Way for Grid Energy Storage. *Adv Energy Mater* **2020**, *10* (32). https://doi.org/10.1002/aenm.202001274.

(8) Peters, J. F.; Cruz, A. P.; Weil, M. Exploring the Economic Potential of Sodium-Ion Batteries. *Batteries* **2019**, *5* (1). https://doi.org/10.3390/batteries5010010.

(9) Ma, B.; Lee, Y.; Bai, P. Dynamic Interfacial Stability Confirmed by Microscopic Optical Operando Experiments Enables High-Retention-Rate Anode-Free Na Metal Full Cells. *Advanced Science* **2021**, *8* (12). https://doi.org/10.1002/advs.202005006.

(10) Hwang, J. Y.; Kim, J.; Yu, T. Y.; Sun, Y. K. A New P2-Type Layered Oxide Cathode with Extremely High Energy Density for Sodium-Ion Batteries. *Adv Energy Mater* **2019**, *9* (15). https://doi.org/10.1002/aenm.201803346.

(11) Billaud, J.; Clément, R. J.; Armstrong, A. R.; Canales-Vázquez, J.; Rozier, P.; Grey, C. P.; Bruce, P. G. β-NaMnO2: A High-Performance Cathode for Sodium-Ion Batteries. *J Am Chem Soc* **2014**, *136* (49), 17243–17248. https://doi.org/10.1021/ja509704t.

(12) Wang, P. F.; You, Y.; Yin, Y. X.; Guo, Y. G. Layered Oxide Cathodes for Sodium-Ion Batteries: Phase Transition, Air Stability, and Performance. *Advanced Energy Materials*. Wiley-VCH Verlag March 15, 2018. https://doi.org/10.1002/aenm.201701912.

(13) Peng, J.; Zhang, W.; Liu, Q.; Wang, J.; Chou, S.; Liu, H.; Dou, S. Prussian Blue Analogues for Sodium-Ion Batteries: Past, Present, and Future. *Advanced Materials*. John Wiley and Sons Inc April 1, 2022. https://doi.org/10.1002/adma.202108384.

(14) Xie, B.; Sun, B.; Gao, T.; Ma, Y.; Yin, G.; Zuo, P. Recent Progress of Prussian Blue Analogues as Cathode Materials for Nonaqueous Sodium-Ion Batteries. *Coordination Chemistry Reviews*. Elsevier B.V. June 1, 2022. https://doi.org/10.1016/j.ccr.2022.214478.

(15) Shang, Y.; Li, X.; Song, J.; Huang, S.; Yang, Z.; Xu, Z. J.; Yang, H. Y. Unconventional Mn Vacancies in Mn–Fe Prussian Blue Analogs: Suppressing Jahn-Teller Distortion for Ultrastable Sodium Storage. *Chem* **2020**, *6* (7), 1804–1818. https://doi.org/10.1016/j.chempr.2020.05.004.

(16) Li, Y.; Gao, Y.; Wang, X.; Shen, X.; Kong, Q.; Yu, R.; Lu, G.; Wang, Z.; Chen, L. Iron Migration and Oxygen Oxidation during Sodium Extraction from NaFeO2. *Nano Energy* **2018**, *47*, 519–526. https://doi.org/10.1016/j.nanoen.2018.03.007.

(17) Mathiyalagan, K.; Shin, D.; Lee, Y. C. Difficulties, Strategies, and Recent Research and Development of Layered Sodium Transition Metal Oxide Cathode Materials for High-Energy Sodium-Ion Batteries. *Journal of Energy Chemistry*. Elsevier B.V. March 1, 2024, pp 40–57. https://doi.org/10.1016/j.jechem.2023.10.023.

(18) Bauer, A.; Song, J.; Vail, S.; Pan, W.; Barker, J.; Lu, Y. The Scale-up and Commercialization of Nonaqueous Na-Ion Battery Technologies. *Adv Energy Mater* **2018**, *8* (17). https://doi.org/10.1002/aenm.201702869.

(19) Jin, T.; Li, H.; Zhu, K.; Wang, P. F.; Liu, P.; Jiao, L. Polyanion-Type Cathode Materials for Sodium-Ion Batteries. *Chemical Society Reviews*. Royal Society of Chemistry April 21, 2020, pp 2342–2377. https://doi.org/10.1039/c9cs00846b.

(20) Deb, D.; Sai Gautam, G. Critical Overview of Polyanionic Frameworks as Positive Electrodes for Na-Ion Batteries. *J Mater Res* **2022**, *37* (19), 3169–3196. https://doi.org/10.1557/s43578-022-00646-7.

(21) Liu, T.; Zhang, Y.; Jiang, Z.; Zeng, X.; Ji, J.; Li, Z.; Gao, X.; Sun, M.; Lin, Z.; Ling, M.; Zheng, J.; Liang, C. Exploring Competitive Features of Stationary Sodium Ion Batteries for Electrochemical Energy Storage. *Energy and Environmental Science*. Royal Society of Chemistry May 1, 2019, pp 1512–1533. https://doi.org/10.1039/c8ee03727b.

(22) Zheng, Q.; Yi, H.; Li, X.; Zhang, H. Progress and Prospect for NASICON-Type Na3V2(PO4)3 for Electrochemical Energy Storage. *Journal of Energy Chemistry*. Elsevier B.V. November 1, 2018, pp 1597–1617. https://doi.org/10.1016/j.jechem.2018.05.001.

(23) Muruganantham, R.; Chiu, Y. T.; Yang, C. C.; Wang, C. W.; Liu, W. R. An Efficient Evaluation of F-Doped Polyanion Cathode Materials with Long Cycle Life for Na-Ion Batteries Applications. *Sci Rep* **2017**, *7* (1). https://doi.org/10.1038/s41598-017-13718-0.

(24) Zhu, C.; Song, K.; Van Aken, P. A.; Maier, J.; Yu, Y. Carbon-Coated Na3V2(PO4)3 Embedded in Porous Carbon Matrix: An Ultrafast Na-Storage Cathode with the Potential of Outperforming Li Cathodes. *Nano Lett* **2014**, *14* (4), 2175–2180. https://doi.org/10.1021/nl500548a.

(25) Tang, X.; Ding, H.; Teng, J.; Zhao, H.; Li, J.; Zhang, K. Green and Scalable Synthesis of Na3V2(PO4)3 Cathode and the Study on the Failure Mechanism of Sodium-Ion Batteries. *ACS Appl Energy Mater* **2023**, *6* (16), 8443–8454. https://doi.org/10.1021/acsaem.3c01195.

(26) Cheng, C.; Zang, X.; Hou, W.; Li, C.; Huang, Q.; Hu, X.; Sun, C.; Zhang, Y.; Yang, J.; Ma, F. Construction of Three-Dimensional Electronic Interconnected Na3V2(PO4)3/C as Cathode for Sodium Ion Batteries. *J Alloys Compd* **2022**, *899*. https://doi.org/10.1016/j.jallcom.2021.163363.

(27) Ling, R.; Cai, S.; Xie, D.; Li, X.; Wang, M.; Lin, Y.; Jiang, S.; Shen, K.; Xiong, K.; Sun, X. Three-Dimensional Hierarchical Porous Na3V2(PO4)3/C Structure with High Rate Capability and

Cycling Stability for Sodium-Ion Batteries. *Chemical Engineering Journal* **2018**, *353*, 264–272. https://doi.org/10.1016/j.cej.2018.07.118.

(28) LI, J. Preparation of Na3V2(PO4)3 Cathode Materials by Hydrothermal Assisted Sol-Gel Method for Sodium -Ion Batteries. *Research and Application of Materials Science* **2024**, *5* (1), 5. https://doi.org/10.33142/rams.v5i1.11757.

(29) Cao, X.; Pan, A.; Yin, B.; Fang, G.; Wang, Y.; Kong, X.; Zhu, T.; Zhou, J.; Cao, G.; Liang, S. Nanoflake-Constructed Porous Na 3 V 2 (PO 4) 3 /C Hierarchical Microspheres as a Bicontinuous Cathode for Sodium-Ion Batteries Applications. *Nano Energy* **2019**, *60*, 312–323. https://doi.org/10.1016/j.nanoen.2019.03.066.

(30) Zeng, X.; Peng, J.; Guo, Y.; Zhu, H.; Huang, X. Research Progress on Na3V2(PO4)3 Cathode Material of Sodium Ion Battery. *Frontiers in Chemistry*. Frontiers Media S.A. July 24, 2020. https://doi.org/10.3389/fchem.2020.00635.

(31) Zhang, B.; Ma, K.; Lv, X.; Shi, K.; Wang, Y.; Nian, Z.; Li, Y.; Wang, L.; Dai, L.; He, Z. Recent Advances of NASICON-Na3V2(PO4)3 as Cathode for Sodium-Ion Batteries: Synthesis, Modifications, and Perspectives. *Journal of Alloys and Compounds*. Elsevier Ltd June 25, 2021. https://doi.org/10.1016/j.jallcom.2021.159060.

(32) Luo, C.; Qiu, R.; Li, G.; Shi, X.; Mao, Z.; Wang, R.; Jin, J.; He, B.; Gong, Y.; Wang, H. Electrospun Na3V2(PO4)3/Carbon Composite Nanofibers as Binder-Free Cathodes for Advanced Sodium-Ion Hybrid Capacitors. *Mater Today Energy* **2022**, *30*. https://doi.org/10.1016/j.mtener.2022.101148.

(33) Luo, L.; Cheng, B.; Chen, Y.; Chen, S.; Liu, G.; Zhuo, H. Electrospun Na3V2(PO4)3/C Nanofibers as Self-Standing Cathode Material for High Performance Sodium Ion Batteries. *Mater Res Express* **2020**, *7* (2). https://doi.org/10.1088/2053-1591/ab6f37.

(34) Luo, L.; Cheng, B.; Chen, S.; Ge, Z.; Zhuo, H. Three-Dimensional Na3V2(PO4)3/Carbon Nanofiber Networks Prepared by Electrospinning as Self-Standing Cathodes for High Performance Na-Ion Batteries. *Mater Lett* **2018**, *232*, 153–156. https://doi.org/10.1016/j.matlet.2018.08.078.

(35) Van Nghia, N.; Jafian, S.; Hung, I. M. Synthesis and Electrochemical Performance of the Na3V2(PO4)3 Cathode for Sodium-Ion Batteries. *J Electron Mater* **2016**, *45* (5), 2582–2590. https://doi.org/10.1007/s11664-016-4425-5.

(36) Li, G.; Jiang, D.; Wang, H.; Lan, X.; Zhong, H.; Jiang, Y. Glucose-Assisted Synthesis of Na3V2(PO 4)3/C Composite as an Electrode Material for High-Performance Sodium-Ion Batteries. *J Power Sources* **2014**, *265*, 325–334. https://doi.org/10.1016/j.jpowsour.2014.04.054.

(37) Zheng, W.; Huang, X.; Ren, Y.; Wang, H.; Zhou, S.; Chen, Y.; Ding, X.; Zhou, T. Porous Spherical Na3V2 (PO4)3/C Composites Synthesized via a Spray Drying -Assisted Process with High-Rate Performance as Cathode Materials for Sodium-Ion Batteries. *Solid State Ion* **2017**, *308*, 161–166. https://doi.org/10.1016/j.ssi.2017.06.012.

(38) Pi, Y.; Gan, Z.; Li, Z.; Ruan, Y.; Pei, C.; Yu, H.; Han, K.; Ge, Y.; An, Q.; Mai, L. Methanol-Derived High-Performance Na3V2(PO4)3/C: From Kilogram-Scale Synthesis to Pouch Cell Safety Detection. *Nanoscale* **2020**, *12* (41), 21165–21171. https://doi.org/10.1039/d0nr04884d.

(39) Zhang, J.; Fang, Y.; Xiao, L.; Qian, J.; Cao, Y.; Ai, X.; Yang, H. Graphene-Scaffolded Na3V2(PO4)3 Microsphere Cathode with High Rate Capability and Cycling Stability for Sodium

Ion Batteries. *ACS Appl Mater Interfaces* **2017**, *9* (8), 7177–7184. https://doi.org/10.1021/acsami.6b16000.

(40) Du, G.; Wang, S.; Zheng, M. 3D CNT Decorated Na3V2(PO4)3/C Microsphere with Outstanding Sodium Storage Performance for Na-Ion Batteries. *Solid State Ion* **2018**, *317*, 229–233. https://doi.org/10.1016/j.ssi.2018.01.028.

(41) Mcconvey, I.; Hoyle, M.; Nulty, O. *REDUCING THE HAZARDS ASSOCIATED WITH SPRAY DRYING FROM LABORATORY THROUGH TO LARGER SCALE INCLUDING CONSIDERATIONS FOR OUTSOURCING AND SECONDARY CONTAINMENT*; 2009.

(42) Chen, L.; Zhao, Y.; Liu, S.; Zhao, L. Hard Carbon Wrapped Na3V2(PO4)3@C Porous Composite Extending Cycling Lifespan for Sodium-Ion Batteries. *ACS Appl Mater Interfaces* **2017**, *9* (51), 44485–44493. https://doi.org/10.1021/acsami.7b14006.

(43) *MSE PRO 50g Ketjenblack EC600JD Conductive Carbon Black for Battery Re– MSE Supplies LLC*. https://www.msesupplies.com/products/mse-pro-50g-ketjenblack-ec600jd-conductive-carbon-black-for-battery-research?variant=39371360731194&gad_source=1&gclid=CjwKCAiA5pq-BhBuEiwAvkzVZRUbp-oZL-5BnSErwwskcGaXjt5PXN4oaIg6zdHtu67_My_sngovRhoC50sQAvD_BwE (accessed 2025-03-03).

(44) Bard, A. J.; Faulkner, L. R. *Electrochemical Methods : Fundamentals and Applications*.

(45) Agrawal, S.; Bai, P. Operando Electrochemical Kinetics in Particulate Porous Electrodes by Quantifying the Mesoscale Spatiotemporal Heterogeneities. *Adv Energy Mater* **2021**, *11* (12). https://doi.org/10.1002/aenm.202003344.

(46) Nanda, J.; Remillard, J.; O'Neill, A.; Bernardi, D.; Ro, T.; Nietering, K. E.; Go, J. Y.; Miller, T. J. Local State-of-Charge Mapping of Lithium-Ion Battery Electrodes. *Adv Funct Mater* **2011**, *21* (17), 3282–3290. https://doi.org/10.1002/adfm.201100157.

(47) Gent, W. E.; Li, Y.; Ahn, S.; Lim, J.; Liu, Y.; Wise, A. M.; Gopal, C. B.; Mueller, D. N.; Davis, R.; Weker, J. N.; Park, J. H.; Doo, S. K.; Chueh, W. C. Persistent State-of-Charge Heterogeneity in Relaxed, Partially Charged Li1−xNi1/3Co1/3Mn1/3O2Secondary Particles. *Advanced Materials* **2016**, *28* (31), 6631–6638. https://doi.org/10.1002/adma.201601273.

(48) Thomas-Alyea, K. E.; Jung, C.; Smith, R. B.; Bazant, M. Z. In Situ Observation and Mathematical Modeling of Lithium Distribution within Graphite. *J Electrochem Soc* **2017**, *164* (11), E3063–E3072. https://doi.org/10.1149/2.0061711jes.

(49) Tian, C.; Xu, Y.; Nordlund, D.; Lin, F.; Liu, J.; Sun, Z.; Liu, Y.; Doeff, M. Charge Heterogeneity and Surface Chemistry in Polycrystalline Cathode Materials. *Joule* **2018**, *2* (3), 464–477. https://doi.org/10.1016/j.joule.2017.12.008.

(50) Ma, B.; Agrawal, S.; Gopal, R.; Bai, P. Operando Microscopy Diagnosis of the Onset of Lithium Plating in Transparent Lithium-Ion Full Cells. *ACS Appl Mater Interfaces* **2022**, *14* (49), 54708–54715. https://doi.org/10.1021/acsami.2c16090.

(51) Liu, J.; Kunz, M.; Chen, K.; Tamura, N.; Richardson, T. J. Visualization of Charge Distribution in a Lithium Battery Electrode. *Journal of Physical Chemistry Letters* **2010**, *1* (14), 2120–2123. https://doi.org/10.1021/jz100634n.

(52) Chueh, W. C.; El Gabaly, F.; Sugar, J. D.; Bartelt, N. C.; McDaniel, A. H.; Fenton, K. R.; Zavadil, K. R.; Tyliszczak, T.; Lai, W.; McCarty, K. F. Intercalation Pathway in Many-Particle LiFePO4 Electrode Revealed by Nanoscale State-of-Charge Mapping. *Nano Lett* **2013**, *13* (3), 866–872. https://doi.org/10.1021/nl3031899.

(53) Nakamura, T.; Watanabe, T.; Kimura, Y.; Amezawa, K.; Nitta, K.; Tanida, H.; Ohara, K.; Uchimoto, Y.; Ogumi, Z. Visualization of Inhomogeneous Reaction Distribution in the Model LiCoO2 Composite Electrode of Lithium Ion Batteries. *Journal of Physical Chemistry C* **2017**, *121* (4), 2118–2124. https://doi.org/10.1021/acs.jpcc.6b12133.

(54) Liu, H.; Kazemiabnavi, S.; Grenier, A.; Vaughan, G.; Di Michiel, M.; Polzin, B. J.; Thornton, K.; Chapman, K. W.; Chupas, P. J. Quantifying Reaction and Rate Heterogeneity in Battery Electrodes in 3D through Operando X-Ray Diffraction Computed Tomography. *ACS Appl Mater Interfaces* **2019**, *11* (20), 18386–18394. https://doi.org/10.1021/acsami.9b02173.

(55) Ma, B.; Bai, P. Fast Charging Limits of Ideally Stable Metal Anodes in Liquid Electrolytes. *Adv Energy Mater* **2022**, *12* (9). https://doi.org/10.1002/aenm.202102967.

(56) Lee, Y.; Bai, P. A Bipolar Separator for Autonomous Suppression of Dendrite Penetration in Zinc Metal Batteries. *J Electrochem Soc* **2023**, *170* (6), 060511. https://doi.org/10.1149/1945-7111/acd8fc.